Full Length Article

Microstructural evolution and transmutation in tungsten under ion and neutron irradiation

Matthew J Lloyd [a,b,h,*], Jack Haley [a,b], Bethany Jim [a], Robert Abernethy [a], Mark R Gilbert [b,a], Enrique Martinez [c,d], Khalid Hattar [e,f], Osman El-Atwani [g,i], Duc Nguyen-Manh [b,a], Michael P Moody [a], Paul A.J. Bagot [a], David E.J. Armstrong [a,**]

[a] *Department of Materials, University of Oxford, Parks Road, Oxford OX13PH, United Kingdom*
[b] *UK Atomic Energy Authority, Culham Science Centre, Abingdon, Oxfordshire OX14 3DB, United Kingdom*
[c] *Department of Mechanical Engineering, Clemson University, Clemson, SC 29634, USA*
[d] *Department of Materials Science and Engineering, Clemson University, Clemson, SC 29634, USA*
[e] *Center for Integrated Nanotechnologies, Sandia National Laboratories, Albuquerque, NM 87185, USA*
[f] *Department of Nuclear Engineering, University of Tennessee, Knoxville, TN 37996, USA*
[g] *Materials Science and Technology Division, Los Alamos National Laboratory, Los Alamos, NM, USA*
[h] *School of Metallurgy and Materials, University of Birmingham, Elm Rd, Birmingham B15 2SE, United Kingdom*
[i] *EED, Pacific Northwest National Laboratory, Richland, WA 99353, United States*

ARTICLE INFO

ABSTRACT

This study aims to compare the effects of neutron and self-ion irradiation on the mechanical properties and microstructural evolution in W. Neutron irradiation at the HFR reactor to 1.67 dpa at 800 °C resulted in the formation of large *Re* and Os rich clusters and voids. The post-irradiation composition was measured using APT and verfified against FISPACT modelling. The measured *Re* and Os concentration was used to create alloys with equivalent concentrations of *Re* and Os. These alloys were exposed to self-ion irradiation to a peak dose of 1.7 dpa at 800 °C. APT showed that self-ion irradiation leads to the formation of small Os clusters, wheras under neutron irradiation large *Re*/Os clusters form. Voids are formed by both ion and neutron irradiation, but the voids formed by neutron irradiation are larger. By comparing the behaviour of W-1.4Re and W-1.4Re-0.1Os, suppression of *Re* cluster formation was observed. Irradiation hardening was measured using nanoindentation and was found to be 2.7 GPa, after neutron irradiation and 1.6 GPa and 0.6 GPa for the self-ion irradiated W-1.4Re and W-1.4Re-0.1Os. The higher hardening is attributed to the barrier strength of large voids and *Re*/Os clusters that are observed after neutron irradiation.

Introduction

The development of reliable, high-performance tungsten-based plasma-facing components (PFCs) for the divertor and first wall of a prototype fusion reactor, requires a detailed understanding of the effects of *Re* and Os solute elements produced by transmutation. Design restrictions due to high operating temperatures and a desire to minimise activation of reactor components severely limits material selection. Pure W is currently the leading candidate material, however, there is a lack of performance data under realistic reactor conditions. Tungsten is chosen primarily due to its high temperature operating window [1], low activation [2], good thermal conductivity and resistance to sputtering under He/H plasma exposure. The combined effects of radiation damage and transmutation result in an increase in the inherent brittleness of W, and in a significant increase in its ductile to brittle transition temperature [3–7], thereby restricting the safe operating window. Precipitation of transmutation products, and the formation of voids and interstitial loops, are major contributors in neutron irradiated material [8–11], but the relative proportions of these features [9] and their impact on material properties is sensitive to a number of irradiation parameters.

Transmutation occurs through a sequence of interactions between the incident neutrons and the material, followed by beta or alpha decay

---

* Corresponding author at: Department of Materials, University of Oxford, Parks Road, Oxford OX13PH, United Kingdom.
** Corresponding author.
E-mail addresses: m.j.lloyd@bham.ac.uk (M.J. Lloyd), David.Armstrong@materials.ox.ac.uk (D.E.J. Armstrong).

of the resulting isotopes. Beta decay of unstable W isotopes results mainly in the production of *Re*, as well as Ta to a lesser extent. Os is produced via neutron absorption and beta decay of *Re* nuclei. The active transmutation pathways in a material depends on the composition, irradiation temperature, the level of isotopic enrichment and the incident neutron energy spectrum. The neutron energy spectrum can vary significantly between different reactors and experiments. The rate of transmutation per dpa of damage is expected to be lower for a DEMO reactor when compared with fission spectrum reactors, due to the high proportion of 14 MeV neutrons which have a lower capture cross section than thermal neutrons. Inventory simulations predict a *Re* production rate of 0.1 at.% / dpa for a DEMO reactor [2]. This rate is much higher in fission test reactors (typically between 1 and 15 at.% / dpa [12] depending on the type of reactor and the position of the sample).

The neutron energy spectrum in irradiation experiments in fission reactors typically contains a high fraction of thermal neutrons such as the High Flux Isotope Reactor (HFIR) [13–17]), which results in a higher ratio of transmutation products to damage in dpa, than would be expected in a fusion reactor. To supress transmutation irradiation experiments have been carried out using neutron shielding (shielded Belgian Test Reactor 2 (BR2) irradiations [3,10,18–24] and HFIR experiments [25,26]), and in reactors with a large fast neutron population (e.g. Joyo [9]). Local modification of the neutron flux by adjacent strongly neutron absorbing materials can also decrease the proportion of thermal neutrons, as in the High Flux Reactor (HFR) irradiations [20,27,28].

Despite the solid solution softening effect of *Re* in unirradiated W [29–32], the precipitation of *Re* under irradiation is detrimental to thermal and mechanical performance [3,18]. At high levels of transmutation, in materials irradiated at HFIR, large needle-shaped *Re/Os* precipitates are observed [13]. Large voids have been observed in materials irradiated under a range of conditions [9,12,17,18,20,28], including in low transmutation rate experiments. In polycrystalline samples irradiated at HFR to 1.67 dpa at 900 °C, with a measured post-irradiation composition of 1.1 and 0.1 at.% *Re* and Os, respectively, *Re/Os*-rich clusters were observed with APT and TEM [27] as well as voids decorated with *Re* and Os [28]. In samples irradiated at BR2 to 1.25 dpa at 800 °C, large needle shaped σ and χ phase precipitates were observed, despite the *Re* and Os concentration being just 2 and 0.2 at.% post-irradiation [18,21]. The precipitates in the BR2 sample are significantly larger (in some cases several hundred nanometres long, compared with 10–20 nm in the HFR sample) and are shown to attach to facetted voids. In both HFR and BR2 samples, the precipitates contain a concentrated *Re* and Os-rich core, surrounded by a diffuse cloud of *Re*.

It is clear from these studies that the features formed under irradiation in W are highly sensitive to the parameters used in the irradiation, but systematically analysing the effects of different conditions with neutron irradiation is challenging. Heavy-ion irradiation is a commonly used surrogate for neutron damage as it does not induce activation of the material and can be used to quickly investigate different irradiation parameters. However, the changes observed under heavy-ion irradiation are often different to those observed after neutron irradiation [33]. In the majority of studies using ion irradiation of W-*Re* alloys, no σ and/or χ phase formation is observed, with the exception of alloys close to the threshold for the formation of sigma phase (~25 at.%*Re*) [34]. The formation of small voids has been observed in some ion irradiated material [33,35–37], and can be enhanced by co-implantation with H/He ions [38]. In 100 dpa Si ion irradiation experiments of W-*Re* alloys containing between 1 and 10 wt.% *Re*, voids were only observed in W-3Re [37], whereas under neutron irradiation the presence of *Re* is thought to supress void formation [39]. More data is available on loop formation, but under neutron irradiation at high doses and at elevated temperatures the number density of loops is significantly lower than the number density of voids [40].

Xu et al. studied the clustering of *Re* and Os in W-*Re*-Os and W-*Re*-Ta alloys after high dose self-ion irradiation at 300 and 500 °C [41,42]. APT was used to show that *Re* clustering was suppressed by the presence of

Os, which preferentially formed small clusters. *Re* clusters were also found to be larger at higher temperatures likely due to enhanced diffusion of point defects. In general, differences between ion and neutron irradiation are thought to be a result of high dose rates and enhanced atomic mixing by displacement damage. The high dose rates limit diffusional processes, whereas ballistic mixing can enhance the dissolution of secondary phases formed as a result of irradiation. This is significant in ion irradiation experiments in which a large number of cascades are in close proximity [43,44]. More work is needed to investigate these effects in W and W-*Re* alloys, including atomistic simulations that can account for transmutation effects.

Computational studies using electronic structure calculations have shown that there exists a strong binding between *Re*/Os solute atoms and fast moving self-interstitial dumbbells in W [45–48]. The rapid three-dimensional migration of W-*Re* mixed-interstitial dumbbells increases the rate of solute transport to point defect sinks [46,48,49]. Atomistic Kinetic Monte Carlo (AKMC) studies of W-*Re* have predicted the formation of *Re*-rich clusters due to the migration of these defects [50–52]. Other studies have highlighted the importance of the vacancy-solute interactions in W-*Re*, with the *Re*-vacancy configuration having the lowest energy. Simulations performed with a cluster expansion Hamiltonian for the W-*Re* system have predicted the formation of small voids decorated with *Re* solute atoms [53]. A solute and concentration dependant Ising model was also used to predict the formation of voids decorated with *Re* and Os transmutation products in Metropolis Monte Carlo simulation [54].

In this study, radiation damage and transmutation were investigated in neutron and heavy-ion irradiated W-(*Re*,Os) alloys. Neutron irradiation produced *Re* and Os directly via neutron absorption. Alloys were produced with the same concentration of *Re* and Os and used for heavy-ion implantation. The properties and microstructural characteristics of the materials was compared using nanoindentation, Atom Probe Tomography (APT) and Transmission Electron Microscopy (TEM).

Methodology

Materials

Single-crystal (SC) bars of commercially pure W, measuring 1 × 1 × 12 mm in size were sourced from Metal Crystals and Oxide Ltd. (Cambridge, UK). The samples were cut into rectangular bars to be used as four-point bend specimens, with the faces cut along the [001] directions, details of which are available in previously published work [55]. In this study, samples irradiated in three different facilities will be discussed, as summarised in Table 1. Samples were made for ion irradiation by arc melting oversized billets which were then machined into rods and cut into 1–2 mm thick discs. The high-purity powders were produced by: ACI (California, US) for W-1.4Re-0.1Os and W-2Re samples and Goodfellow (Huntingdon, UK) / AEE (New Jersey, US) for W-1.4Re. Samples were ground and polished with SiC paper of progressively finer grade and diamond paste to a 1 μm finish, before polishing with colloidal silica to achieve a stress-free surface suitable for implantation. The microstructure of the arc-melted samples consists of large grains approximately 100 μm in diameter, meaning that on the scale of the measurements performed in this study, the material can be considered single crystal. APT of the W-*Re*-Os alloys before irradiation found no evidence of clustering.

Neutron irradiation

Neutron irradiation was performed at the High Flux Reactor at Petten, Netherlands to a dose of 1.67 dpa over a total of 208 full power days in two reactor positions. Further details of the irradiation are available in previous published work [27]. Irradiation was carried out for 148 and 60 full power days, providing a neutron flux of 6.8×10^{18} m^{-2} s^{-1} (3.2×10^{18} m^{-2} s^{-1} $E > 0.1$ MeV) and 6.6×10^{18} m^{-2} s^{-1} (3.2×10^{18} m^{-2} s^{-1}

Table 1

Summary of the sample compositions and irradiation conditions used in this study. Doses for the ion implanted materials is taken as the maximum dose at the Bragg peak calculated using SRIM whereas neutron doses are through-thickness.

Facility	Composition (at.%)		Incident Particle	Energy (MeV)	Peak Dose (dpa)	Flux (m^{-2}s^{-1})	Fluence (m^{-2})	T_{irr} (°C)	Time (s)	Peak Dose Rate (dpa/s)	Ref.
	Re	Os									
JANNuS	1.4	–	W^{9+}	24	1.70	7.06×10^{14}	8.1×10^{18}	800	1.16×10^4	1.47×10^{-4}	–
SNL	1.4	0.1	W^{2+}	8	1.70	2.80×10^{14}	3.0×10^{17}	900	1.07×10^3	1.59×10^{-3}	–
SNL	2	–	W^{2+}	8	1.70	2.80×10^{14}	3.0×10^{17}	900	1.07×10^3	1.59×10^{-3}	–
HFR (FISPACT)	1.4	0.1	n	N/A	1.67	$6.6–6.8 \times 10^{18}$	1.21×10^{26}	900	1.8×10^7	9.28×10^{-8}	–
HFR (APT)	1.3	0.1	n	N/A	1.67	$6.6–6.8 \times 10^{18}$	1.21×10^{26}	900	1.8×10^7	9.28×10^{-8}	–
SIBC	1	1	W$^+$	2	33.0	3.06×10^{14}	2.5×10^{19}	500	8.17×10^4	4.04×10^{-4}	[42]
SIBC	25	–	W$^+$	2	33.0	3.06×10^{14}	2.5×10^{19}	500	8.17×10^4	4.04×10^{-4}	[42]

$E > 0.1$ MeV) in each location, respectively. The specimen temperature was controlled during irradiation using a gas-mixture technique. FISPACT-II simulations were performed using a displacement threshold energy of 55 eV for W to calculate the damage in dpa, as outlined in [56]. The level of transmutation predicted by FISPACT-II was 1.4 at.%Re and 0.1 at.%Os, compared with a measured concentration of 1.26 ± 0.15 at.% Re and 0.08 ± 0.02 at.%Os [27]. The level of transmutation was reduced due to the local absorption of thermal neutrons. Irradiation conditions are summarised in Table 1. The measured and predicted compositions are given for the neutron irradiated material [27,28].

Ion irradiation

Irradiation was carried out in two facilities: 1) the Joint Accelerators for Nano-science and Nuclear Simulation, CEA Saclay Frane (JANNuS) and 2) the 6 MV HVE Tandem Accelerator at Sandia National Laboratories, USA (SNL). For each irradiation the dose was estimated using calculations performed with the 2013 version of the Stopping Range of Ions in Matter (SRIM) program. To enable comparison between previous studies, calculations were made using a standard approach to estimating the damage with SRIM, using the "*Ion distribution and Quick calculation of damage*" mode with a lattice binding energy of 0 eV, and a minimum of 10,000 incident ions. Due to the range of displacement threshold energies used in the literature, SRIM calculations were performed using

different values from the literature: 55, 68 and 90 eV A value of $E_d = 55$ eV was used in the calculation of the dose for the neutron irradiated material using FISPACT. The E_d given in ASTM E521 for W is 90 eV [57]. The peak dose varies between 1.7 and 1.0 dpa, as shown in Fig. 1, depending on the value of E_d used. The dose in dpa was estimated using the sum of the vacancies produced by incident ions and recoils in the vacancies output file. The difference in peak dose produced by different E_d highlights an important source of uncertainty between irradiation experiments. Table 1 summarises the irradiation conditions used in each experiment and includes data on previously published self-ion irradiations for comparison. Approximate irradiation times are included for W-1Re-1Os material irradiated at the Surrey Ion Beam Centre and was calculated from the provided flux and fluence values [54]. Note that the dose in these materials was calculated using full-cascade mode, whereas the dose in the JANNuS and SNL samples was determined using SRIM in "quick calculation of damage" mode. Irradiation temperature for the HFR samples is approximate and was controlled during irradiation using a gas-mixture technique

It is well understood that the damage level from SRIM calculations varies depending on the calculation method used. In the present study, the quick calculation method is used to enable comparison between previous studies. For comparison, running SRIM in full-cascade mode following the method outlined by Agarwal et al. [58] gives a peak dose of around 3.1 dpa. For these calculations a lattice binding energy of
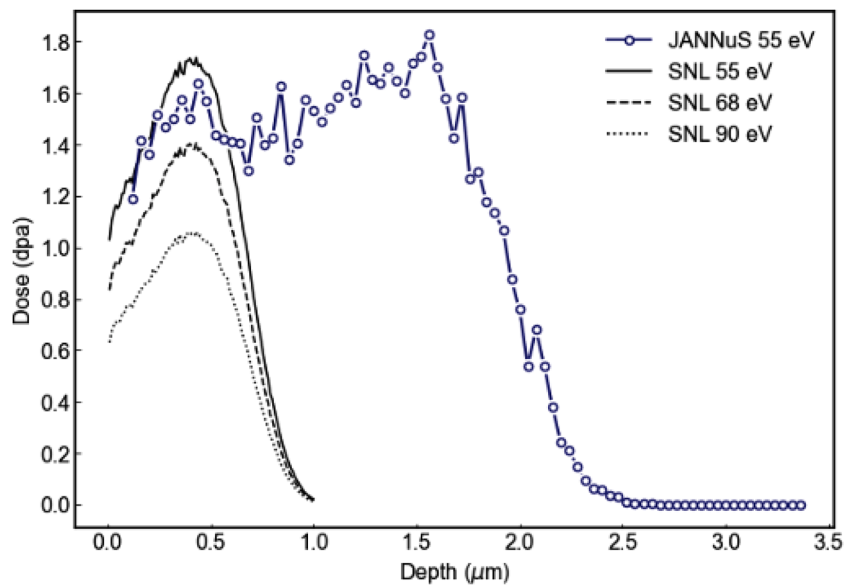

Fig. 1. Dose as a function of depth into the sample surface estimated for the self-ion irradiation experiments SNL and JANNuS. Dose profiles were calculated using SRIM, in Quick Kinchin Pease mode, with a lattice binding energy of 0 eV and three displacement threshold energies, E_d: 55 eV, 68 eV and 90 eV, obtained from different literature sources for W.

13.654 eV was used, as the sum of the formation energies for a $\langle 111 \rangle$ self-interstitial atom (10.086 eV) and a vacancy (3.568 eV) in W. A displacement threshold energy of 55 eV was used and the dose in dpa was estimated using the Norgett-Robinson-Torrens (NRT) model which relates the number of Frenkel pairs generated in a cascade to the energy transferred in elastic collisions, and E_d. The energy transfer T_{dam} was calculated as a function of depth using by subtracting the phonon energy produced by the incident ion from the phonon energy produced by recoil ions, both of which are output in the phonon output file.

From this point onwards, the dose received by each sample will be discussed in terms of those calculated using 55 eV using the quick cascade method. This enables comparison with the neutron irradiated material as well as previously published ion irradiation studies. It should be noted however that full cascade SRIM calculations give a damage level approximately 1.8 times higher than those conducted in the quick mode.

A sample with a composition of W-1.4 at.%*Re* was irradiated at JANNuS with W^{9+} ions accelerated to 24 MeV using a 3 MV Pelletron accelerator (Épiméthée). Aluminium degrader foils of varying thickness were used to flatten out the irradiation profile and provide a damage plateau at approximately 1.7 dpa, as shown in Fig. 1. Irradiation was carried out at a temperature of 800 °C, with a total ion flux of 7.0×10^{14} $m^{-2}s^{-1}$, over an implantation time of 11,580 s or around 3.5 h.

W-1.4Re-0.1Os and W-2Re samples were implanted at SNL using 8 MeV, W^{2+} ions. A Bragg peak of 1.7 dpa was predicted at approximately 450 nm into the sample surface, as shown in Fig. 1. Irradiation was carried out at a temperature of 900 °C which was achieved using a button heater mounted on the underside of the specimen during implantation. The temperature of the sample was monitored using an annular thermocouple mounted on the edge of the specimen. The ion beam had a circular spot that was positioned in the centre of the specimen during implantation. The position of the beam relative to the specimen was not translated during irradiation. Analysis was performed on samples taken from the centre of the specimen. A total flux of 2.8×10^{14} $m^{-2}s^{-1}$ was achieved over an implantation time of 1071s or approximately 30 min. The range in dose at the Bragg peak calculated using different displacement threshold energies from the literature are summarised in Table 2.

Nanoindentation

Nanoindentation was performed using a G200 Nanoindenter (XLS, USA) with a Berkovich diamond indenter calibrated against fused silica. The continuous stiffness measurement (CSM) mode was used, which allows the hardness and elastic modulus to be determined as a function of depth by imposing small, high-frequency oscillation [59]. An oscillation of 2 nm at 45 Hz was used. Indents were made to 2000 nm final depth at a target indentation strain rate of $0.05 \ s^{-1}$ ($\dot{\varepsilon} = dh \ /h$ where h is indenter displacement). Arrays of 25 indents were performed for each sample and condition. Irradiation hardening was calculated at 500 nm for comparison between different samples. Although the measurement of nanohardness may vary with grain orientation in W [60] it is small compared to the hardening observed due to irradiation, as such the effect of orientation has not been explored in this study.

Table 2
Peak doses at the Bragg peak calculated using SRIM, using the "Ion distribution and Quick calculation of damage" mode with a lattice binding energy of 0 eV, and a minimum of 10,000 incident ions for the SNL irradiation, using 3 different settings for the displacement threshold energy, E_d.

Displacement Threshold Energy (eV)	Dose at Bragg Peak (dpa)
55	1.70
68	1.40
90	1.06

Atom probe tomography

APT specimens from both ion and neutron irradiated samples were produced using a standard Focussed Ion Beam (FIB) lift-out procedure. For the ion implanted samples, this was performed using a dual beam Zeiss NVision FIB-SEM, at the University of Oxford's David Cockayne Centre for Electron Microscopy (DCCEM), equipped with a Kleindeik Nanotechnik W manipulator. For the neutron irradiated specimen, sample activity required the use of remote handling facilities at the Materials Research Facility (MRF), United Kingdom Atomic Energy Authority (UKAEA). The lift-out was performed using a dual beam FEI Helios FIB-SEM, equipped with an Oxford Instruments Omniprobe. A protective layer of C or Pt was first deposited on the surface of the samples, between 1 and 1.5 μm thick, in order to provide contrast during thinning. Trenches were milled using an acceleration voltage of 30 kV and a beam current of 3 nA. The cantilever was then undercut using these same conditions. The cantilever was then joined to a Cameca 22 post silicon microcoupon array, using GIS deposited W or Pt as a binding material.

For the ion implanted specimens, the APT needles were shaped using a range of successively lower beam currents between 700 pA and 10 pA until a cross section of approximately <100 nm was achieved at the contrast boundary between the carbon protective layer and W sample. A 2 kV, 300 pA beam was then used to polish the carbon protective layer away from the surface and remove a depth of the sample which depends on the implantation condition. In each of the ion irradiated samples, the samples were polished using this beam condition to the approximate location of the Bragg peak. The neutron irradiated samples were sharpened until <75 nm in diameter at the tip, as a greater degree of loss from the surface was acceptable. In the neutron irradiated samples, the tip of the sample was made at <500 nm depth from the surface of the sample to remove any surface effects. As before, a 2 kV, 300 pA polishing stage was then applied to remove Ga implantation from the surface.

APT was carried out using a Cameca LEAP 5000-XR. Samples were loaded into the load lock chamber within 12 h of removal from the FIB and were left for >12 h before proceeding to the higher vacuum buffer chamber. Samples were analysed in laser mode using a laser beam energy of 100 pJ, a specimen temperature of 55 K and a pulse frequency of 100 kHz. The detection rate was varied between 1% and 0.1% depending on the tip and lowered in some cases to improve ion yield. Reconstruction of the data was done using IVAS version 3.8.4, using a voltage mode reconstruction method.

Transmission electron microscopy (TEM)

TEM foils were prepared via the FIB lift-out method [61] at the UKAEA Materials Research Facility. To remove 30 kV Ga+ FIB damage, for final thinning 5 kV and 2 kV Ga+ was used; however, this was insufficient to adequately remove dislocation-type FIB-damage in the ion-irradiated sample, and also introduced curtaining artefacts to the foil. This meant the ion irradiated foil was not suitable for irradiation-induced dislocation analysis, but analysis of voids was still possible.

TEM imaging of voids was conducted at DCCEM, Oxford using a JEOL 2100 L LaB$_6$ source and 200 kV accelerating voltage. Voids were imaged using the under/over-focus technique [62], and capturing a focal series between −2 μm and +2 μm in steps of 500 nm. Images at ±500 nm were used for sizing voids, whereas all images were used to aid counting voids. Images were captured far from a strong two-beam condition, but - specifically for the ion-irradiated sample - diffraction contrast from preparation artefacts (curtaining and FIB-induced dislocations) remained strong in comparison to the voids. In order to accurately identify small voids within the ion-irradiated sample, the remaining diffraction contrast in the images was suppressed by producing a new image from the difference between the under and over-focus images. Since the contrast of voids is inverted in

under/over-focus pairs, the difference between these images enhances the contrast of voids, while suppressing background contrast due to diffraction. An issue with this approach is that the subtle change in magnification due to differences in the objective lens strength is enough to shift the relative positions of voids in the micrograph, resulting in the difference-image appearing distorted at the edges. To correct for this, the magnification of the under- and over-focus pairs were corrected via an affine-transform alignment to the in-focus condition [63]. A demonstration of these steps is shown within the provided supplementary material. The large voids of the neutron-irradiated sample were much more clearly visible than those in the ion-irradiated sample, and so these steps were not required.

Foil thicknesses were measured via Electron Energy Loss Spectroscopy (EELS), using a JEOL ARM200F equipped with a cold Field Emission Gun (FEG) operating at 200 kV, and Quantum Gatan Imaging Filter (GIF). Convergence and collection half angles were 31.5 mrad and 41.0 mrad, respectively. The log-ratio method was used to compute the thickness from zero-loss spectra [64,65]. Voids were characterised according to their volume fraction, F, calculated as $\Delta V / V_i$.

Results

Irradiation hardening

Fig. 2 shows the hardness as a function of depth for indents in W-1.4Re and W-1.4Re-0.1Os before and after ion irradiation to 1.7 dpa at 800 °C and 900 °C, respectively, as well as the hardening produced by neutron irradiation of single crystal W at HFR. Hardening can be observed in both ion implanted samples with the W-1.4Re sample from JANNuS having the highest hardening of the two. To compare between samples, the hardness was measured before and after irradiation at an indenter displacement of 500 nm. This depth corresponds to the approximate location of the Bragg peak in the SNL sample where the dose is 1.7 dpa. The dose at 500 nm in the JANNuS sample is approximately 1.5 dpa, but there is uncertainty in the SRIM data due to the use of different degrader foils.

In the neutron irradiated material the dose of 1.67 dpa is constant with depth. The hardness at 500 nm is summarised in Fig. 3. In the

unirradiated condition the hardness of each of the materials is roughly equivalent - the W-1.4Re has a slightly higher hardness (5.7 GPa) compared to the W-1.4Re-0.1Os (5.5 GPa) and pure-W (5.5 GPa), but these values are within the measurement uncertainty. Following irradiation, the neutron irradiated material experienced the greatest hardening $\Delta H = 2.7$ GPa, increasing from 5.5 to 8.2 GPa. In the W-1.4Re sample the hardening was also significant but not as high as in the neutron irradiated material at $\Delta H = 1.6$ GPa, increasing from 5.7 to 7.3 GPa. By comparison, the hardening measured in the W-1.4Re-0.1Os sample was lower at $\Delta H = 0.6$ GPa, increasing from 5.5 GPa to 6.1 GPa after irradiation.

Transmutation

Mass peak identification in APT data relies on manual peak ranging and labelling of peaks in the resulting spectra. The standard approach to separating the contributions to an individual mass peak, is to use the heights of the adjacent non-overlapping mass peaks to determine the ratio of the elements in the peak. This is possible because the heights of the peaks for a particular element are distributed according to the natural abundance for that element. The dynamic production and consumption of isotopes during neutron irradiation results in a different distribution of isotopes. As discussed in our previous work, mass peak labelling and ranging must therefore rely on inventory calculations to identify overlaps in the mass spectrum.

Fig. 4 shows a portion of the mass spectrum between 58 and 65 Da containing the W^{3+}, Re^{3+}, Os^{3+} and Ta^{3+} ions. The coloured regions highlight the peaks corresponding to different elements. Fig. 4(a) shows data from the neutron irradiated specimen (W-1.3Re-0.1Os), whereas (b) and (c) data from the JANNuS (W-1.4Re), SNL (W-1.4Re-0.1Os) samples, respectively. The spectrum shown in (d) is from a W-1Re-1Os sample ion irradiated at the Surrey Ion Beam Centre (SIBC) to a peak dose of 33 dpa by Xu et al., and is included here for comparison [42]. For the spectra shown in (a) and (c) which have a similar composition, there is a clear difference between the position and relative intensities of the *Re* and Os peaks. Because the samples shown in Fig. 4(b), (c) and (d) were alloyed prior to ion irradiation, the isotopes are distributed according to the natural abundances of each isotope, as shown in Table 3.
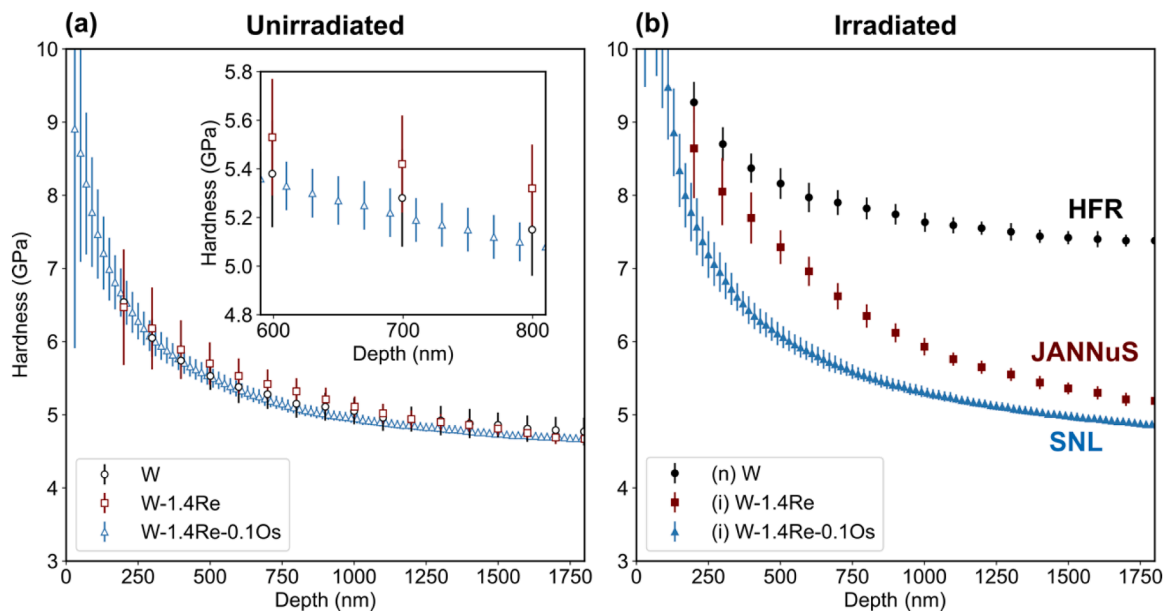

Fig. 2. Average hardness versus displacement curves for indentations during continuous stiffness measurement (CSM) mode in (a) unirradiated W and W alloys and (b) ion and neutron irradiated W and W alloys. Indentation data is plotted for unirradiated single crystal W before and after neutron irradiation at HFR, and polycrystalline, arc-melted W-1.4 at.% *Re* and W-1.4 at.%- 0.1 at.%Os before and after heavy-ion implantation at JANNuS and SNL, respectively. In the post-irradiation condition, the *Re* and Os concentration in the neutron irradiated W sample was 1.3 at.%*Re* and 0.12 at.%Os.
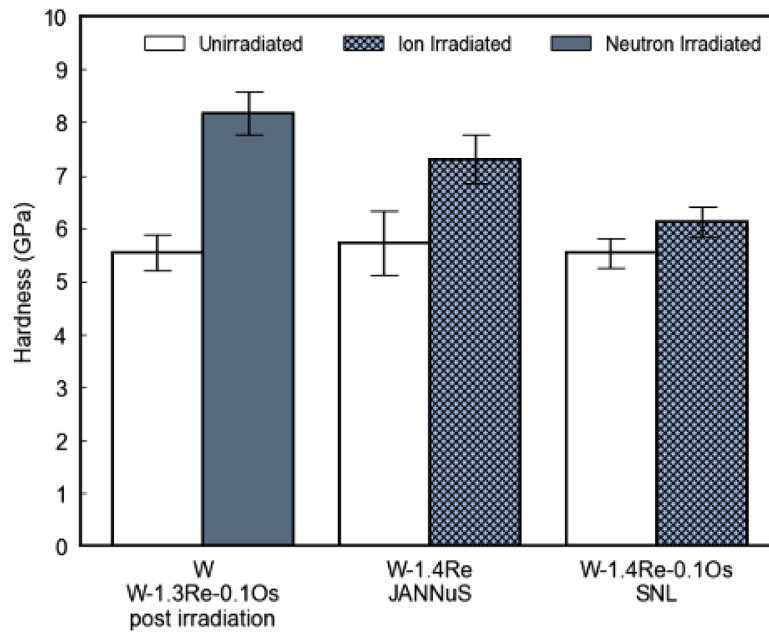
Fig. 3. Hardness values for neutron irradiated single crystal tungsten and self-ion implanted W-1.4Re and W-1.4Re-0.1Os from JANNuS and SNL, measured at 500 nm indentation depth.
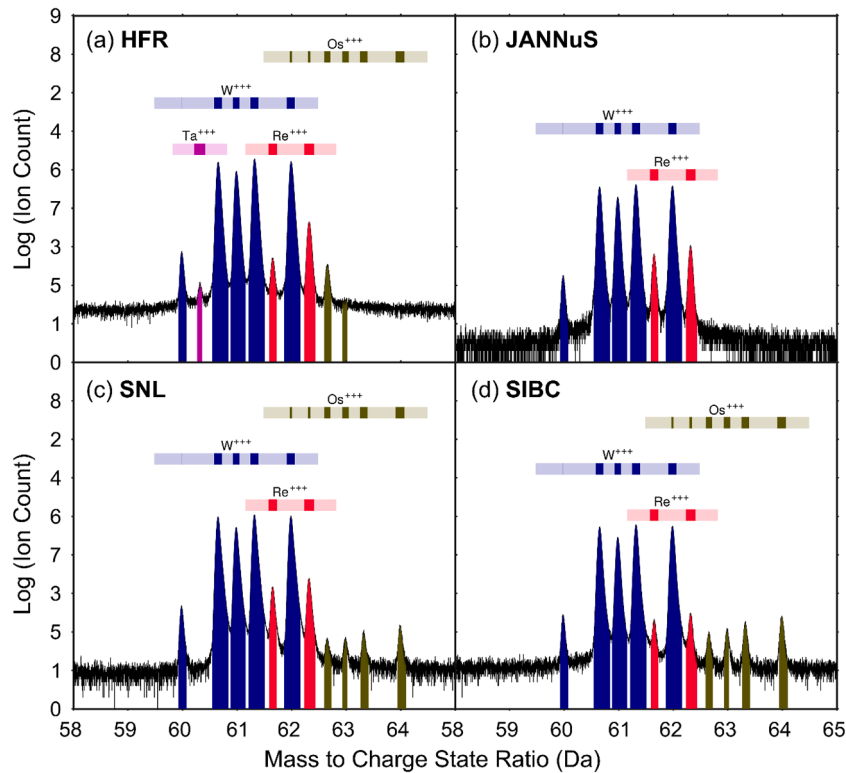

Fig. 4. Portion of the APT mass spectra between 58 and 65 Da, showing the 3+ charge state ions taken from (a) HFR neutron irradiated (b) W-1.4Re JANNuS ion irradiated (c) W-1.4Re-0.1Os SNL ion irradiated and (d) W-1Re-1Os sample ion irradiated at the Surrey Ion Beam Centre (SIBC) to a dose of 33 dpa [46]. Each mass peak is coloured according to the ranged element and the bar above indicates the relative isotopic natural abundances. The thicker the coloured bar above the mass peak, the higher the abundance of that isotope.

The bars plotted above the peaks in Fig. 4 show the expected peak positions and relative intensities for each element, which for (b), (c) and (d) align with the ranged peaks. Only minimal overlap is expected between the ^{186}Os and ^{187}Os peaks with ^{186}W and ^{187}Re, respectively. As the proportion of the Os atoms expected to be ^{186}Os and ^{187}Os is only 1.59 and 1.60%, respectively, and the overall concentration of Os is 0.1, and 1 at.% for the samples shown in (c) and (d), deconvolution of the peaks was not performed as the Os contribution to the 62 and 62.3 Da peaks is negligible.

To compare the distribution of isotopes, each peak was ranged as a

Table 3

Comparison between neutron and ion irradiated specimens from SNL and HFR, showing isotopic abundances compared with the natural abundance of each isotope in unirradiated W [2]. Undetectable refers to isotopes that were predicted in small quantities by FISPACT but were below the detection limit of APT within the volume of material analysed. Uncertainty in the measured isotopic concentration from APT is estimated by comparing the values at under and over ranged mass peak ranges.

Nuclide	Natural Abundance (%) [2]	Measured Abundance (%)			
		SNL	HFR (Single Crystal)	HFR (Polycrystalline)	FISPACT (%)
^{180}W	0.12	0.12 ± 0.01	0.11 ± 0.01	0.11 ± 0.01	0.10
^{182}W	26.50	27.08 ± 0.59	25.32 ± 0.57	26.32 ± 0.38	25.79
^{183}W	14.31	14.09 ± 0.36	15.53 ± 0.48	14.32 ± 0.65	15.21
^{184}W	30.64	32.02 ± 1.47	32.26 ± 0.76	33.39 ± 2.16	31.45
^{186}W	28.43	26.68 ± 1.70	26.77 ± 0.68	25.85 ± 1.77	27.45
^{185}Re	37.40	37.19 ± 0.40	8.36 ± 0.93	9.17 ± 0.72	9.33
^{187}Re	62.20	62.81 ± 0.40	91.64 ± 0.93	90.83 ± 0.72	90.67
^{184}Os	0.02	Undetectable	Undetectable	Undetectable	<0.01
^{186}Os	1.59	Undetectable	Undetectable	Undetectable	<0.01
^{187}Os	1.60	Undetectable	Undetectable	Undetectable	<0.01
^{188}Os	13.29	15.36 ± 4.80	99.64 ± 0.38	94.88 ± 1.85	92.24
^{189}Os	16.21	18.97 ± 0.51	0.64 ± 0.38	5.12 ± 1.85	1.76
^{190}Os	26.36	25.21 ± 2.16	Undetectable	Undetectable	0.11
^{192}Os	40.93	40.45 ± 4.27	Undetectable	Undetectable	<0.01

separate species using IVAS. The concentrations are summarised in Table 3. Two ranging approaches were used to estimate the uncertainty introduced by different techniques. Each mass peak was ranged from background-to-background, and using a narrow region at the peak. The concentration given by these two extreme cases was used to determine the range of concentration for each element or isotope. This uncertainty was then combined with the counting error by adding in quadrature. For onward analysis of segregation of these elements the peaks were ranged
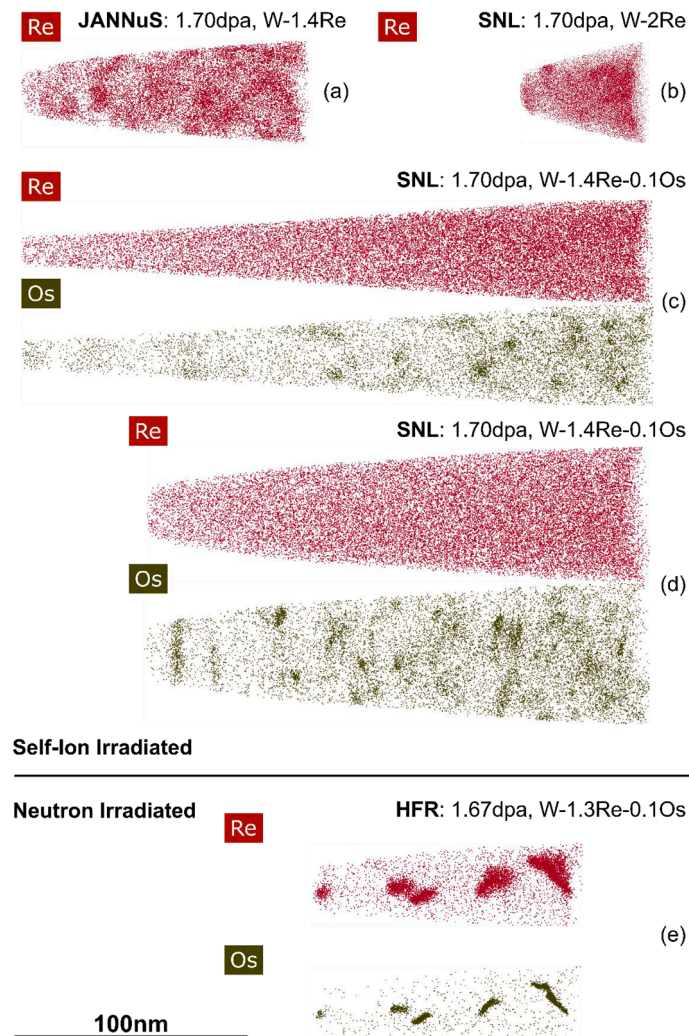

Fig. 5. APT reconstructions showing *Re* (red) and Os (green) atoms from neutron and ion irradiated W-*Re*-Os with a dose of 1.7 dpa. (a)-(d) show different ion irradiated materials whereas (e) shows a reconstruction from the neutron irradiated material from HFR.

7

at approximately the full-width at half maximum.

For the SNL sample in which transmutation did not occur, the measured abundances are in agreement with the expected natural abundances. For the neutron irradiated sample the W isotopes are also largely in agreement with the natural abundances, with a slight depletion of ^{186}W measurable. The large resonance peak in ^{186}W makes it a particularly strong neutron absorber. For the *Re*, 90% of the measured ions are ^{187}Re, whereas in the SNL sample this is just 60%, likely due to the high neutron absorption efficiency of ^{186}W, which initiates the transmutation to ^{187}Re. The neutron absorption cross sections of ^{186}W and ^{184}W are shown in provided in the appendix. Transmutation to ^{187}Re and ^{185}Re occurs via the neutron absorption of ^{186}W and ^{184}W, followed by the beta decay of the products, ^{187}W and ^{185}W, both of which are unstable with half-lives of 23.8 h and 75.1 days, respectively. The large absorption resonance, and higher overall cross section at low neutron energies of ^{186}W result in a higher rate of ^{187}Re production. In natural Os sample, only 13.3% of the Os atoms are ^{188}Os. As shown in Table 3 the ratio between Os isotopes in the SNL sample agree with the natural abundances. In the neutron irradiated material the ^{188}Os is between 94 and 99% of the Os ions detected. A small amount of ^{189}Os ions were detected, though in the single crystal material the number of these ions was very small. As such the percentage of ^{189}Os ions in the single crystal material cannot be distinguished from the background.

Re and Os clustering

In all of the samples analysed in this study, clustering of *Re* and/or Os was observed. Fig. 5 shows a comparison of the *Re* and Os clustering between ion and neutron irradiated material, all irradiated to a dose of 1.7 dpa. All of the reconstructions are plotted using the same scale bar to highlight the differences in cluster sizes. Full atom maps are used without cropping the data, and use red and green spheres with a radius of 0.1 nm to show the positions of *Re* and Os atoms respectively. Comparing Fig. 5(a) and (b), which show W-1.4Re and W-2Re irradiated at JANNuS and SNL to 1.70 dpa, there is clearly a tendency for *Re* to form clusters. The samples show in (a) and (b) were irradiated at SNL, at 1073 and 1173 K respectively. The *Re* concentration is enriched in some regions and depleted in others, rather than forming distinct, spherical clusters. In the ion irradiated materials containing Os, *Re* clusters does not occur and the clusters that form consist primarily of Os, as shown in Fig. 5(c) and (d). Os clustering occurs preferentially to *Re* despite the lower bulk composition (0.1 at.% Os compared with 1.4 at.%*Re*). Fig. 5 (c) and (d) both show the same sample with 1.4 at.% *Re* and 0.1 at.%Os, but are taken at different depths from the specimen surface. The needle shown in Fig. 5(c) was taken from a shallower depth than (d) but it is not possible to determine exactly the depth from which it was obtained.

In the neutron irradiated sample shown in Fig. 5(e), the clusters contain both *Re* and Os atoms, exhibiting a central *Re*/Os core surrounded by a diffuse cloud of *Re* atoms. Fig. 6 highlights the difference in the clustering behaviour of *Re* between the neutron irradiated sample from HFR and the W-1.4Re sample irradiated at JANNuS. The clusters are highlighted by isoconcentration surfaces plotted at 3, 5 and 10 at.% *Re* for each sample. At a contour concentration of 5 at.% and above, the regions highlighted in the JANNuS are no longer visible, indicating that the internal concentration of these clusters is below 5 at.%*Re*. For the HFR sample, the clusters are clearly visible even at 10 at.% *Re* isoconcentration surfaces. The reduction in *Re* isoconcentration surface size at increasing *Re* concentrations, shows that there is a diffuse boundary between the enriched and depleted regions. As highlighted in previous work, the internal concentration of the clusters may in some instances exceed 50 at.%*Re* in the neutron irradiated HFR sample. For the JANNuS sample, the interface between the clusters and the bulk is more diffuse and the exact boundary between individual clusters is harder to distinguish. Some of the *Re* concentrated regions appear interlinked, rather than as discrete clusters.

To provide a measure of the difference in cluster composition under irradiation with ions and neutrons, the compositions of the clusters were analysed using a standard maximum separation method (MSM) [66]. When using a MSM to study cluster compositions, the region from which the concentration is calculated is determined independently for each cluster, based on a set of parameters. These parameters were optimised for each material and then applied to multiple data sets using the posgen program, within the APTTools software package. This method defines a boundary between cluster and matrix using this set of parameters. The cluster concentration is then calculated using all of the atoms contained within this boundary.

This method relies on the assumption that a pair of Nearest Neighbour (NN) solute atoms within a cluster are separated by a distance, d_{max}, less than their counterparts in the matrix. The maximum separation distance d_{max} was estimated using the nearest neighbour distribution of Os atoms in the SNL and Surrey samples. The value of d_{max} was chosen at the NN distance of maximum difference between the sample data and a complementary spatially randomised dataset. The same approach was applied to the cluster subtracted data to check whether any clustering was still measurable. A minimum cluster size N_{min} (in terms of the number of atoms), was also defined using a histogram of experimental and spatially randomised data. N_{min} was defined at the cluster size at which the randomised distribution falls to zero counts. An envelope distance, L, was set to $d_{max}/2$ and an erosion distance, d_e, defined as approximately L/2. Once optimised for the ion irradiated samples, similar parameters were then applied to the neutron irradiated samples. The optimised parameters used in each data set analysis are
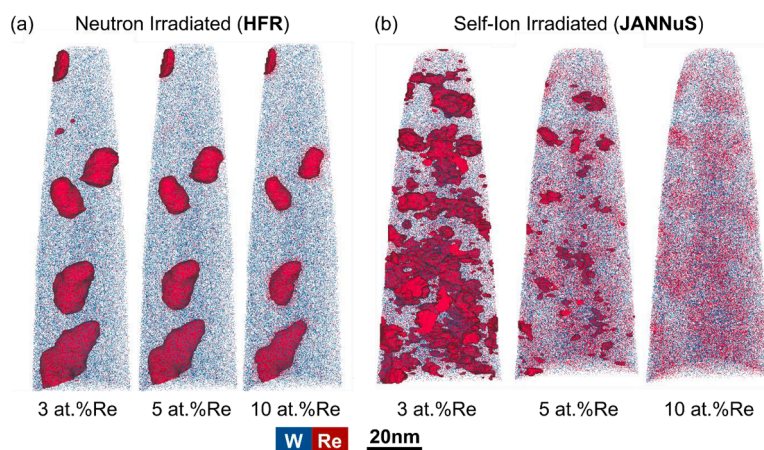

(a)   Neutron Irradiated (**HFR**)   (b)   Self-Ion Irradiated (**JANNuS**)

3 at.%Re   5 at.%Re   10 at.%Re   3 at.%Re   5 at.%Re   10 at.%Re

W   Re   20nm

Fig. 6. *Re* isoconcentration surfaces plotted at 3, 5 and 10 at.%*Re* for the neutron irradiated sample from HFR on the left and the ion irradiated W-1.4at.%*Re* sample ion irradiated at JANNuS on the right.

summarised in Table 4.

To compare the segregation mechanisms between the ion and neutron irradiated materials, the *Re* and Os concentrations for each cluster is plotted in Fig. 7. This enables us to study the correlation between *Re* and Os atoms inside the clusters. The composition was obtained using the MSM with the parameters shown in Table 5. This method does not distinguish between decorated voids and *Re/*Os clusters, as both features appear as *Re/*Os concentrated regions in the APT reconstruction. Each datapoint shown in Fig. 7 corresponds to a different *Re/*Os rich region identified using the MSM. For illustrative purposes, the size of each datapoint is scaled by the size of the *Re/*Os rich region identified in the APT dataset measured using the radius of gyration. The trajectory aberrations induced by voids means that a quantitative analysis of the cluster sizes is not currently possible. For comparison Fig. 7 also includes clusters from a W-1Re-1Os sample ion irradiated to a peak dose of 33 dpa at 500 °C [42]. It should be noted that 33 dpa was calculated using the full-cascade mode in SRIM which typically overestimates the damage level when compared with the quick mode.

In the ion irradiated material, the Os concentration inside the clusters is higher with a fairly constant *Re* concentration. The clusters formed in the SNL sample are more highly concentrated in Os, despite the fact that the bulk concentration of the sample is a factor of 10 smaller. Fig. 7 shows that there are differences in composition between the SNL and HFR samples. The clusters formed in the HFR sample are much larger than under ion irradiation to the sample dose and have a higher *Re* concentration. In the HFR sample, clusters with a higher *Re* concentration also have a higher Os concentration. This trend is not clearly observed in the ion irradiated materials.

The composition of the clusters in the neutron irradiated sample is consistent with the solid solution bcc region of the W-*Re*-Os phase diagram [67]. It should be noted however that the slow kinetics of these materials means that low temperature data on the equilibrium phases is limited. However, APT was performed on the as-received W-1.4Re-0.1Os sample which also showed no clustering of *Re* or Os. As we have highlighted in previous publications [27] the clusters formed under neutron irradiation have a higher concentration of *Re* and Os in their centre compared with the periphery. The composition returned by the maximum separation algorithm is therefore sensitive to the location of the boundary between cluster and matrix.

Void formation

During APT of the neutron irradiated material, high density artefacts in the reconstructed APT data were indicative of voids [28,68]. These artefacts are areas in the reconstructed APT data created when the trajectory of ions from the specimen are deflected due to changes in the tip morphology [69]. High density regions in reconstructed APT data have been used to identify the positions of voids and He bubbles, therefore enabling quantification of segregation to the surface [70–74]. Specimen inhomogeneity can also lead to variations in reconstructed atomic density and care must be taken interpreting these features without complimentary techniques.

APT of the ion implanted materials was performed and atomic density isosurfaces were used to map variations in atomic density. Using this approach, abnormally high density regions were observed in the neutron irradiated material which are indicative of voids. In the ion irradiated materials no significant density artefacts were observed in the reconstructed volume. This suggested that no voids were present in the
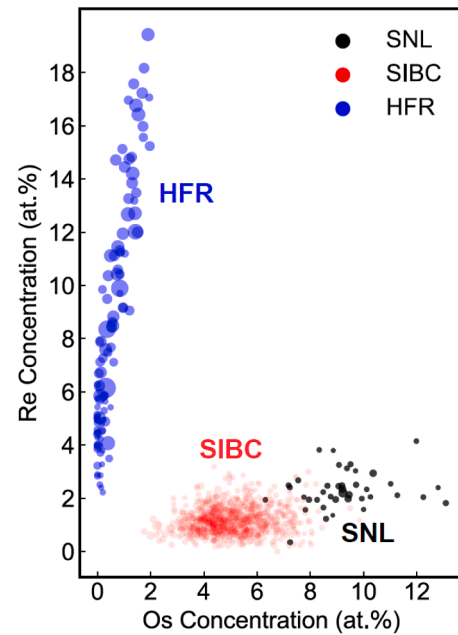
Table 4
Optimised parameters used for quantification of clusters using MSM.

Sample	d_{max}	N_{min}	L	d_e	Ref.
HFR	1	20	0.7	0.25	This study
SNL	1	13	0.5	0.25	This study
SIBC	1.1	20	0.7	0.3	[42]

Fig. 7. Ratio of *Re* to Os concentration in clusters formed in ion and neutron irradiated W, determined using a MSM. Points plotted in blue correspond to clusters formed under neutron irradiation in the HFR sample, after 1.67 dpa at 900 °C. Red and black points both represent clusters formed during ion irradiation. Red points are clusters from W-1Re-1Os sample irradiated to 22 dpa at SIBC at 500 °C [42]. The black points correspond to clusters in W-1.4Re-0.1Os irradiated to 1.7 dpa at 900 °C at SNL. The points are scaled by their radius of gyration.

volume of material sampled by APT, but TEM showed that small voids (~1–2 nm) were present in the material. The inter-void spacing in Fig. 8 shows that either no voids are present in the APT data or that small voids formed by ion irradiation were not large enough to induce ion trajectory aberrations that are visible after reconstruction. The impact of voids on the reconstruction of APT data would benefit from correlative TEM measurements.

This is something that was commonly observed in the neutron irradiated material. Fig. 8 shows a comparison between the voids observed under ion and neutron irradiation at SNL and HFR, respectively (further images of these are provided as supplementary material). As observed in previous studies, the neutron irradiated sample contains larger voids (~5–10 nm). Voids formed under ion irradiation are considerably smaller at the same irradiation temperature, dose and *Re/*Os concentration. As summarised in Table 1, the dose rate used in the SNL irradiation is four orders of magnitude higher than the dose rate of the neutron irradiation experiment. Achieving a peak dose of 1.7 dpa took less than an hour at SNL, whereas the neutron irradiation took place over 208 days (~5000 h). In the SNL sample, void sizes were correlated with the dose received at different depths. Fig. 9 shows a stitched TEM image at different depths from the sample surface. The lower right-hand side of the image corresponds to the approximately 300 nm from the original sample surface. The depth from the original sample surface increases towards the upper left-hand side of the image. The volume fraction of voids is plotted as a function of depth in Fig. 10 alongside the calculated dose profile from SRIM. It shows that the highest volume fraction occurs at the approximate position of the Bragg peak where the dose is highest.

Discussion

Nanoindentation measurements showed that before irradiations there was little difference in hardness between the SC pure W and W-*Re/*W-*Re*-Os alloys. Because the hardness of SC W is expected to be lower than that of polycrystalline material, it is possible that the *Re* and Os has

Table 5

Summary of average *Re* and *Os* concentrations, x_{Re} and x_{Os} inside clusters formed under neutron irradiation at HFR and ion irradiation at SNL and SIBC. The standard deviation in the average concentrations of *Re* and *Os*, σ_{Re} and σ_{Os}, are also given. The average cluster size is given in terms of the total number of ranged ions in the cluster, N_T, and in terms of the radius of gyration, r_g, given by the cluster search algorithm.

Sample	*Re* (at.%)	Os (at.%)	Dose (dpa)	T_{irr}	x_{Re}	σ_{Re}	x_{Os}	σ_{Os}	N_T	r_g	Ref.
HFR	1.3	0.1	1.70	900	7.23	4.42	0.36	0.50	26,979	4.3	This Study
SNL	1.4	0.1	1.70	900	2.32	0.72	9.28	1.52	473	1.6	This study
SIBC	1.0	1.0	33.0	500	1.18	0.51	5.12	1.18	828	1.6	[42]
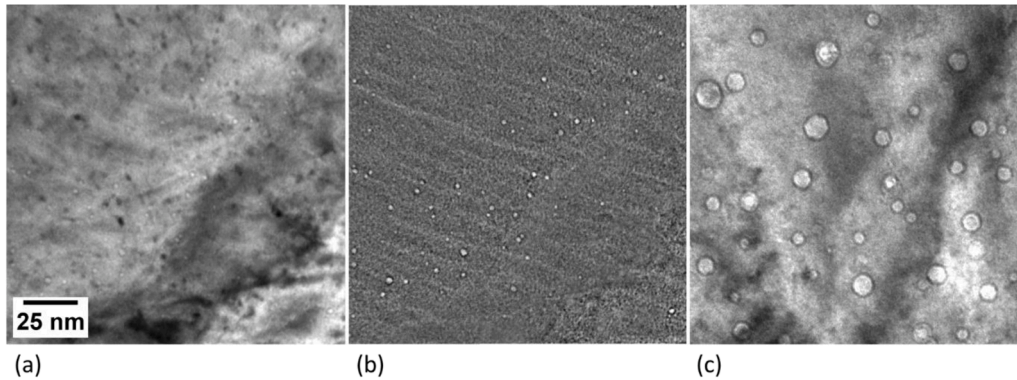
Fig. 8. Comparison between voids formed in W-1.4Re-0.1Os by ion irradiation and by neutron irradiation. Images (a) and (b) show the same regions of the ion irradiated sample (irradiated at SNL to a dose of 1.7 dpa at 900 °C). Image (a) is captured at −500 nm defocus, and (b) depicts the difference between defocus conditions +500 nm and −500 nm (see methods section). Image (c) shows the initially pure, single crystal W (neutron irradiated at HFR to a dose of 1.67 dpa at 900 °C) with a post irradiation composition of W-1.3Re-0.1Os, with a defocus of −1500 nm. Images are plotted on the same scale and voids are visible as bright regions.

had some solid solution softening effect. It should be noted that measurements performed using Vickers indentation in single crystalline tungsten typically results in lower hardness when compared with polycrystalline materials [75]. Under irradiation, the presence of *Re* and Os causes hardening in the material due to the formation of clusters. The highest hardening occurs in the neutron irradiated material, which is consistent with the microstructural characterisation. The microstructure contains large voids, and dense *Re/*Os-rich clusters, both of which are barriers to dislocation movement. Compared to voids, previous analyses of the SC sample also found a lower number density of ⟨111⟩ loops in the SC sample, (10^{20} m^{-3} compared with 10^{21} for voids) [27]. According to the Dispersed Barrier Hardening (DBH) model, the change in hardness is proportional to where N is the number density of defects and d is the average diameter. The smaller voids observed in the ion implanted material result in less hardening, which is consistent with the DBH model. Comparing the contributions to hardening from *Re/*Os clusters and precipitates is more challenging due to differences in the composition and the diffuse nature of the cluster/matrix interface. In addition to the size difference, small precipitates likely form in the centre of the *Re* rich zones in the neutron irradiated material which would affect the barrier strength.

In the self-ion irradiated samples, the highest hardness was in the W-1.4Re followed by the W-1.4Re-0.1Os. By contrast, Xu et al. observed that 1 at.% Os caused an increase in hardening following self-ion irradiation to 33 dpa. This could suggest that the smaller and less concentrated Os clusters shown in Fig. 5, and the small voids shown in Fig. 9, are weaker obstacles than those observed by Xu et al. However, it is difficult to compare between these studies due to the different implantation depths. The Bragg peak depth in these samples was only 125 nm which could also have introduced surface effects due to sample preparation or indentation size effects which may have affected the hardness measurements. A deeper understanding of the effect of Os requires a systematic investigation of different alloy compositions under equivalent conditions.

There are microstructural similarities between these samples and the W-1Re-1Os samples irradiated by Xu et al. Here we observe that Os

supresses the formation of the *Re* clusters that can be seen in the W-1.4Re sample. Here we observe this effect with an Os concentration of just 0.1 at.%.

Comparing hardening between the W-*Re* and W-*Re*-Os samples, nanoindentation shows that the Os clusters formed in the W-1.4Re-0.1Os sample cause less hardening than the *Re* enriched regions formed in the W-1.4Re sample. The JANNuS sample has a deeper Bragg peak depth than the SNL samples (see Fig. 1). The region of plastic deformation below the indent is larger than the displacement of the indenter, which means for a shallow indent the hardness measured is affected by both irradiated and unirradiated material. At lower depths the response from the SNL and JANNuS samples are similar but deviate at greater depths.

Hardening in the neutron irradiated materials is clearer higher, despite the same composition. This is due to the larger voids and clusters in the neutron irradiated material. Furthermore the clusters formed by neutron irradiation are likely to be stronger barriers to dislocation movement. In addition to being larger, there may be precipitation of an incoherent sigma phase in the centre of these clusters which would also inhibit dislocations. There is no evidence to suggest that the sigma has precipitated in the *Re/*Os rich regions produced by ion irradiation under the present conditions.

The causes of the differences between neutron and ion irradiated materials are not easy to ascertain due to the large number of variables involved in performing irradiation experiments. Here we have attempted to minimise the number of variables by using samples with a similar *Re* and Os concentration and have irradiated the materials to an equivalent dpa, at the same irradiation temperature. Therefore, we hypothesise that the differences in the ion and neutron irradiated materials are a result of 1) the difference in dose rate, 2) the occurrence of ballistic dissolution in the ion irradiated material and 3) the occurrence of transmutation reactions in the neutron irradiated material.

A key difference between the segregation observed in these alloys and those which undergo conventional radiation-induced segregation (RIS) is the occurrence of transmutation reactions. In the case of the neutron irradiated W studied here, the segregating elements *Re* and Os
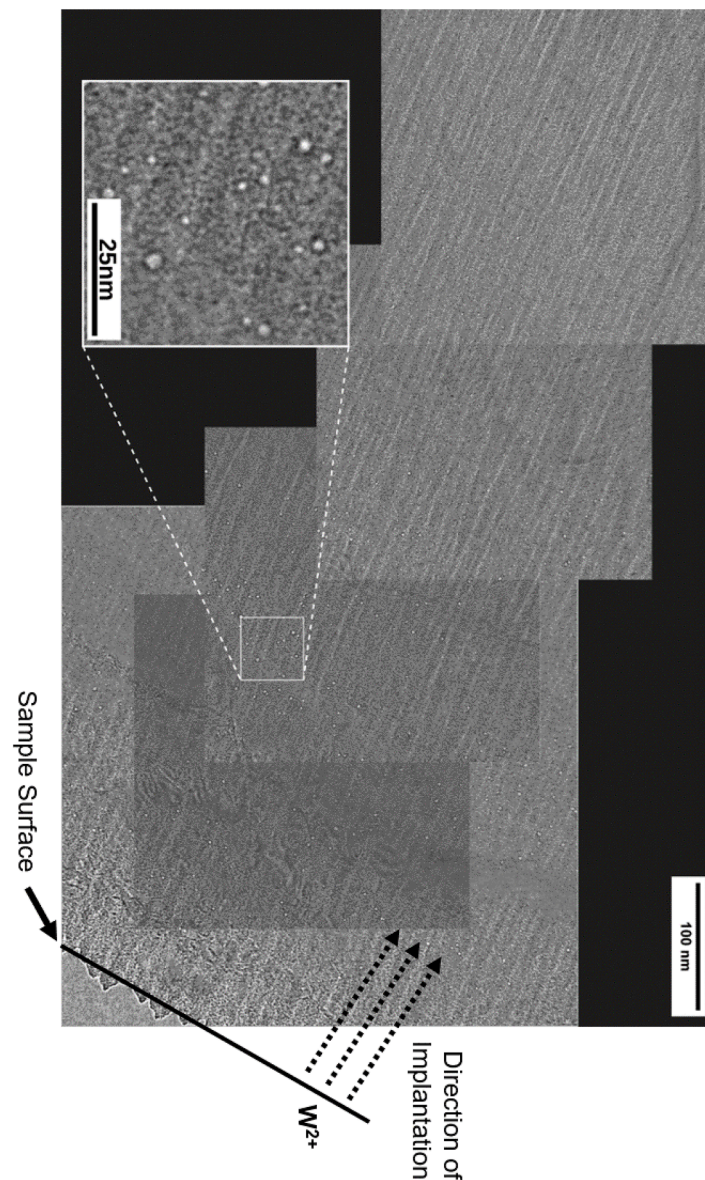
Fig. 9. Stitched TEM images at different depths into the sample surface, showing voids in bright contrast. The surface of the foil, corresponding to a depth of approximately 300 nm from the original sample surface, is in the bottom right of the image. The number density of voids is $\sim 10^{22}$ m^{-3}, with a maximum ~ 8-9×10^{22} m^{-3} ~ 300–400 nm from the surface.

are produced continuously via transmutation during irradiation, unlike the ion irradiated samples which have a constant *Re* and Os concentration during irradiation. Therefore in the neutron irradiated material the hardening is associated with the strength of transmutation induced segregation via the interaction of *Re* and Os atoms with both vacancies and self-interstitial atoms. This leads to a very high activation barrier of dissolution of *Re* and Os from clusters even at very high temperatures.

Calculations of the transport coefficients between *Re*/Os and vacancies/SIAs predict solute drag can occur for *Re* except at very high temperatures. This points towards a very strong tendency for both elements to diffuse towards point defect sinks including grain boundaries, voids, small *Re*/Os clusters and dislocation loops. The transport coefficient is stronger for Os than for *Re*, suggesting that Os atoms may preferentially undergo diffusion, limiting the number of defects available to drag *Re* atoms. The presence of Os is correlated with an increase in hardening under irradiation in the neutron irradiated sample. The Os-vacancy interaction strength is higher than the *Re*-vacancy interaction which could also contribute to an increase in hardness. This is supported by previous DFT calculations [76].

The clusters formed in the neutron irradiated material consist of a denser core of *Re* and Os atoms surrounded by a diffuse cloud of *Re*, as shown in Figs. 5 and 6. The size and composition of the clusters also vary significantly, as summarised in Fig. 7. The core is typically around 10 nm in length, and is rod shaped in some instances. However, some clusters are roughly spherical. Differences between the clusters in the ion and neutron irradiated material can be seen visually in Fig. 5. For both W-*Re* and W-*Re*-Os the clusters are smaller and more diffuse than those seen in the neutron irradiated sample and do not contain an enriched core. It is possible that by continuing to increase the dose in the ion irradiation experiments *Re*/Os precipitates could form in the growing clusters with increasing point defect creation and diffusion. However, it is not clear from the current data if this growth would be balanced by dissolution via ballistic mixing and diffusive transport away from sinks. Further studies are required to fully understand the competing mechanisms behind *Re*/Os cluster formation under these conditions.

Table 5 compares the sizes and compositions of the clusters formed under neutron and ion irradiation. In the binary W-1.4Re and W-2Re samples from JANNuS and SNL, *Re* enrichment occurs. Unlike higher
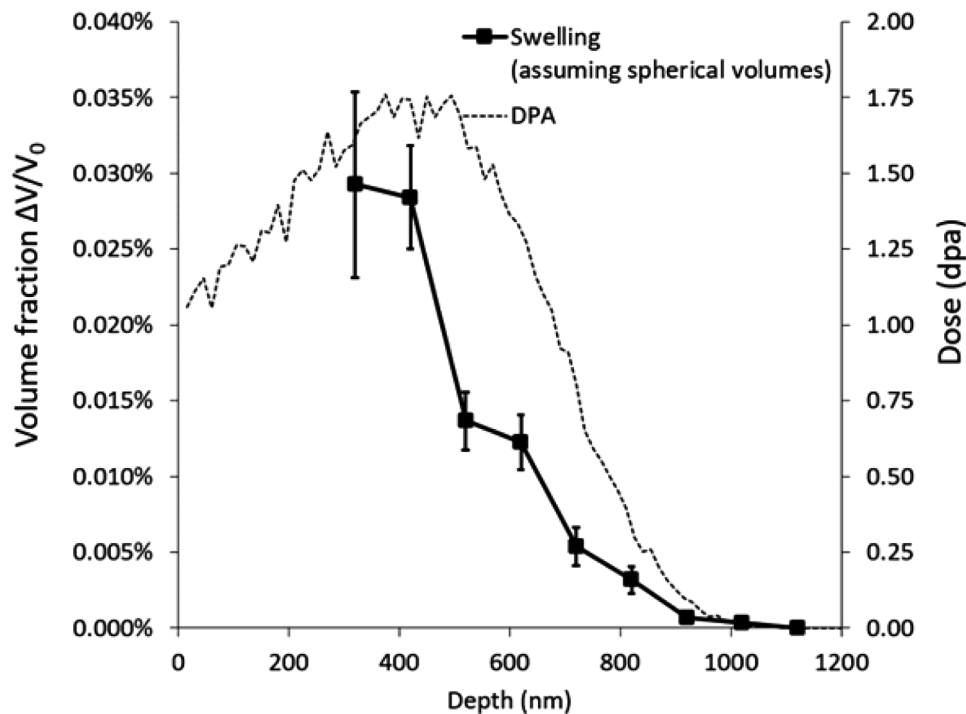
Fig. 10. Volume fraction of voids in the ion implanted W-1.4Re-0.1Os sample irradiated at SNL, plotted as a function of depth into the sample surface. Overlaid is the calculated dose vs depth profile from SRIM. The uncertainty in each volume fraction point is a propagation of the uncertainty in sizing voids from the TEM images.

dose self-ion irradiation experiments carried out by Xu et al. in W-2Re, the *Re* does not form distinct, spherical clusters [41,42]. It is possible that at higher doses there is a greater concentration of point defects to transport the solute atoms to clusters, however, the effects of dose are thought to saturate above a certain dpa. Xu et al. found that in heavy-ion irradiation experiments with a dose as high as 33 dpa that *Re/*Os clusters formed, but not the secondary phases seen in neutron irradiation experiments. The effects on cluster formation therefore saturate above some dose under ion irradiation. The underlying reasons for this would benefit from dedicated experimental studies and atomistic simulations using different dose rates and defect concentrations.

As summarised in Table 1, there is a difference of around four orders of magnitude in the irradiation time, and hence dose rate, between the SNL and HFR samples. This difference is indicative of most ion and neutron irradiation experiments. Both the formation of voids, and *Re/*Os clusters are controlled by the diffusion of point defects.

Void and cluster formation depend on diffusion and are therefore sensitive to the irradiation temperature. Examination of samples neutron irradiated at different temperatures found larger voids formed at 800 °C than at 600 °C or 1000 °C [77]. Higher temperatures generally increase diffusion and therefore promote the growth of larger voids. At higher temperatures the concentration of supersaturated vacancies decreases thus decreasing the flux of vacancies to voids and preventing further growth [78].

Despite the significant difference in dose rates, Os clustering was still observed in the SNL sample, however, the clusters were smaller and had a different composition to that of the HFR sample. *Re* migration is thought to be associated with the diffusion of the W-*Re* mixed interstitial dumbbell. The high irradiation temperature used throughput the experiments in this study would promote diffusion of *Re* and Os, but relatively small clusters and voids were observed in the ion implanted materials. The small clusters in the ion irradiated material could be due to the distribution of sinks in the material. *Re* and Os clusters can be formed by mixed interstitial clustering, which can subsequently act as point defect sinks. Vacancy clusters, interstitial atom clusters and dislocations could all act as sinks for point defects around which

enrichment could occur. If a high number density of sinks were formed, there would be a large number of potential destinations for diffusing *Re/*Os atoms and the lower the enrichment would be at each sink. A high dose rate could have led to such a distribution by preventing the clustering of defects. It is challenging to conduct systematic neutron irradiation experiments at different dose rates and temperatures. Ion irradiation experiments at different temperatures and dose rates, and/or atomistic modelling could be performed to understand whether this hypothesis impacts *Re/*Os cluster formation.

The presence of *Re* may also affect the point defect concentration in the material. *Re* is understood to promote recombination of vacancies and interstitials in collision cascades [46,47,79,80]. This is the mechanism by which alloying W with *Re* can decrease swelling [39] and supress vacancy cluster growth [81]. Self-interstitial atoms move via one-dimensional migration, whereas the W-*Re* mixed interstitial dumbbell undergoes three-dimensional migration through a sequence of translations and rotations. As a result, separation between interstitials and vacancies following a cascade decreases, thus increasing recombination. This results in a decrease in vacancy concentration, therefore supressing vacancy clustering [46].

Under neutron irradiation the cascades occur in pure W before the build up of *Re* through transmutation. This occurs in W via neutron absorption and subsequent beta decays. The *Re* alloying additions in the ion irradiated material will promote recombination and therefore decrease swelling. This may also affect cluster formation by decreasing the concentration of point defects that enable diffusion. This may therefore contribute to smaller clusters and voids in the ion irradiated material.

Os formation occurs primarily as a result of neutron absorption and beta decay of *Re* atoms. The results shown in Fig. 7 suggest that Os may have formed directly inside *Re* enriched regions such as in clusters or at the periphery of voids. Alternatively the Os may have formed by interaction with *Re* atoms in solution and undergone diffusion to these clusters.

In the ion irradiated specimen, Os shows a stronger tendency to form clusters than *Re*. In this case the Os is initially dissolved along with *Re* in

the W. The tendency to form clusters in this instance is likely therefore due to the stronger binding of Os atoms to both interstitials and vacancies. This then supresses *Re* cluster formation due to the preferential formation of Os clusters. In the W-*Re* alloy it is clear that *Re* clustering is still favourable under these conditions. Both transmutation inside *Re* clusters and preferential diffusion contribute to the strong Os segregation observed under neutron irradiation.

The addition of Os inside the *Re* clusters may help to accelerate the formation of intermetallics under neutron irradiation. This could explain why the clusters in the neutron irradiated material consist of a diffuse *Re* cloud with a more concentrated core. A similar structure with a *Re* cloud and a central precipitate has also been observed in samples irradiated at the BR2 reactor [18,21].

The data plotted in Fig. 7 shows the ratio of *Re* to Os concentration inside the clusters. In the ion irradiated samples, the clusters compositions are distributed around an average value. The clusters formed by neutron irradiation have a linear relationship. The higher the *Re* concentration inside a cluster, the higher the Os concentration. This supports the idea that transmutation occurs inside the clusters. Fitting the data for the neutron irradiated sample gives the following relationship between *Re* and Os concentration: $x_{Re} = 7.1x_{Os} + 0.045$

Simulating neutron irradiation of W using ion irradiation remains challenging. Transmutation reactions occur under neutron irradiation due to the interaction of neutrons with isotopes of the material. In this study we have used alloying to introduce representative quantities of *Re* and Os prior to irradiation. It is possible that the *Re* and Os alloying will also affect the irradiation response by increasing vacancy interstitial recombination during cascades, and by affecting the diffusion of point defects. *Re/Os* ions could be injected directly into the sample to create point defects and simulate transmutation reactions. Achieving the correct ratio between dose and transmutant concentration observed under neutron irradiation would be highly challenging.

Ballistic dissolution under ion irradiation is also known to affect phase stability and cluster formation. The diffuse interface of the clusters in the SNL and JANNuS samples could be a result of cascades which continuously disrupt the structure of the clusters. Ballistic effects could also affect the number density of sinks, preventing large point defect clusters from growing thus suppressing the enrichment of *Re* and Os. Ballistic mixing in the ion irradiated material may have contributed to the dilute concentration inside the clusters are therefore prevented the formation of intermetallic phases which are observed under neutron irradiation.

Void formation is directly affected by the diffusion of vacancies. The high dose rate used in the ion irradiation means that less time is available for vacancy migration, and therefore smaller voids are observed, as shown in Fig. 8. The overlap between cascades and vacancy clusters or voids may also decrease their size. The results shown in Fig. 10 confirm that the void size is coupled with the excess vacancy concentration, which is higher at the Bragg peak depth. The results suggest that void size is correlated with the dose received by the material. In the present study, it was not possible to characterise *Re* and Os segregation to voids due to the small size, and low *Re* and Os concentrations, but the voids likely act as sinks for point defects and therefore sites where *Re/Os* would be enriched. Atomic density artefacts in the APT data can be indicative of voids, but no such aberrations were observed in the visualisations reconstructed from the SNL data.

We have demonstrated that there are clear differences between the clusters and voids formed under ion and neutron irradiation, even in materials with equivalent *Re/Os* concentrations and irradiated to equivalent damage levels at the same irradiation temperature. The causes of these differences are not yet fully understood, but here we suggest that the difference in dose rates, the effects of ballistic mixing and the occurrence of transmutation reaction under neutron irradiation all contribute to these differences. More work is needed investigate the competing roles of these effects on the formation of voids, precipitates and dislocation loops, as well as the relative strengths at different dose

rates and temperatures. It is clear from the microstructural comparison that differences in the clustering of *Re* and Os, and the formation of voids play a major role in the degradation of mechanical properties under irradiation. The features formed by ion irradiation are different to that of neutron irradiation under the conditions explored in this study, but if caution is taken ion irradiation may still provide a useful tool for the screening of different irradiation environments and material systems.

Conclusion

In this study we have investigated the effects of radiation damage and transmutation reactions on the microstructural evolution of W under neutron and self-ion irradiation. Neutron irradiation at HFR was used to induce *Re/Os* production directly via neutron absorption and beta decay of the resultant isotopes. The concentration of *Re* and Os was measured using APT and was used to create alloys with equivalent concentrations of *Re* and Os. Using this approach we were able to separate the effects of each element, and compare with the neutron irradiated material.

Large clusters of *Re* and Os formed under neutron irradiation which consist of a *Re* and Os rich core surrounded by a diffuse cloud of *Re* atoms. Self-ion irradiation on the other hand led to the formation of small Os clusters. Void formation was observed in both samples, but the voids formed under neutron irradiation were larger. By comparing the behaviour of W-1.4Re and W-1.4Re-0.1Os, suppression of *Re* cluster formation was observed.

Our results suggest that differences between ion and neutron irradiation are the result of different dose rates, ballistic dissolution and transmutation reactions. High dose rates and ballistic dissolution in the ion irradiated materials prevents the growth of large voids and clusters. Transmutation reactions in the neutron irradiated specimen could lead to the formation of Os within *Re* rich regions such as clusters or void surfaces, enhancing the stability of precipitates. Neutron irradiation produced a higher hardening than ion irradiation, which is attributed to the barrier strength of large voids and *Re/Os* clusters.

Declaration of competing interest

The authors declare that they have no known competing financial interests or personal relationships that could have appeared to influence the work reported in this paper.

Acknowledgements

Supplementary materials

Supplementary material associated with this article can be found, in the online version, at doi:10.1016/j.mtla.2023.101991.

References

[1] S.J. Zinkle, N.M. Ghoniem, Operating temperature windows for fusion reactor structural materials, Fusion Eng. Des. 51-52 (2000) 55–71, https://doi.org/10.1016/S0920-3796(00)00320-3.

[2] M.R. Gilbert, J.C. Sublet, R.A. Forrest, Handbook of activation, transmutation, and radiation damage properties of the elements simulated using FISPACT-II & TENDL-2014, Magnet. Fusion Plants (2015) 1–696. Ccfe-R(15)26.

[3] E. Gaganidze, A. Chauhan, H.C. Schneider, D. Terentyev, B. Rossaert, J. Aktaa, Effect of irradiation temperature on the fracture-mechanical behaviour of tungsten irradiated to 1 dpa, J. Nucl. Mater. 556 (2021) 153200, https://doi.org/10.1016/J.JNUCMAT.2021.153200.

[4] R.G. Abernethy, J.S.K.L. Gibson, A. Giannattasio, J.D. Murphy, O. Wouters, S. Bradnam, L.W. Packer, M.R. Gilbert, M. Klimenkov, M. Rieth, H.C. Schneider, C. D. Hardie, S.G. Roberts, D.E.J. Armstrong, Effects of neutron irradiation on the brittle to ductile transition in single crystal tungsten, J. Nucl. Mater. 527 (2019) 151799, https://doi.org/10.1016/J.JNUCMAT.2019.151799.

[5] D. Terentyev, M. Rieth, G. Pintsuk, J. Riesch, A. Von Müller, S. Antusch, K. Mergia, E. Gaganidze, H.C. Schneider, M. Wirtz, S. Nogami, J. Coenen, J.H. You, A. Zinovev, W. Van Renterghem, Recent progress in the assessment of irradiation effects for in-vessel fusion materials: tungsten and copper alloys, Nucl. Fusion 62 (2022), https://doi.org/10.1088/1741-4326/ac4062.

[6] C. Yin, D. Terentyev, S. Van Dyck, A. Stankovskiy, R.H. Petrov, T. Pardoen, Effect of high-temperature neutron irradiation on fracture toughness of ITER-specification tungsten, Phys. Scr. 2020 (2020) 014052, https://doi.org/10.1088/1402-4896/AB54D7.

[7] S. Nogami, D. Terentyev, A. Zinovev, C. Yin, M. Rieth, G. Pintsuk, A. Hasegawa, Neutron irradiation tolerance of potassium-doped and rhenium-alloyed tungsten, J. Nucl. Mater. 553 (2021) 153009, https://doi.org/10.1016/J.JNUCMAT.2021.153009.

[8] X. Hu, Recent progress in experimental investigation of neutron irradiation response of tungsten, J. Nucl. Mater. 568 (2022) 153856, https://doi.org/10.1016/J.JNUCMAT.2022.153856.

[9] X. Hu, T. Koyanagi, M. Fukuda, N.A.P.K. Kumar, L.L. Snead, B.D. Wirth, Y. Katoh, Irradiation hardening of pure tungsten exposed to neutron irradiation, J. Nucl. Mater. 480 (2016) 235–243, https://doi.org/10.1016/j.jnucmat.2016.08.024.

[10] A. Dubinko, D. Terentyev, C. Yin, W. Van Renterghem, B. Rossaert, M. Rieth, E. E. Zhurkin, A. Zinovev, C.C. Chang, S. Van Dyck, G. Bonny, Microstructure and hardening induced by neutron irradiation in single crystal, ITER specification and cold rolled tungsten, Int. J. Refract. Metals Hard Mater. 98 (2021) 105522, https://doi.org/10.1016/J.IJRMHM.2021.105522.

[11] G. Bonny, M.J. Konstantinovic, A. Bakaeva, C. Yin, N. Castin, K. Mergia, V. Chatzikos, S. Dellis, T. Khvan, A. Bakaev, A. Dubinko, D. Terentyev, Trends in vacancy distribution and hardness of high temperature neutron irradiated single crystal tungsten, Acta Mater. 198 (2020) 1–9, https://doi.org/10.1016/J.ACTAMAT.2020.07.047.

[12] A. Hasegawa, M. Fukuda, K. Yabuuchi, S. Nogami, Neutron irradiation effects on the microstructural development of tungsten and tungsten alloys, J. Nucl. Mater. 471 (2016) 175–183, https://doi.org/10.1016/j.jnucmat.2015.10.047.

[13] P.D. Edmondson, B. Gault, M.R. Gilbert, An atom probe tomography and inventory calculation examination of second phase precipitates in neutron irradiated single crystal tungsten, Nucl. Fusion 60 (2020), https://doi.org/10.1088/1741-4326/abb149.

[14] T. Hwang, A. Hasegawa, K. Tomura, N. Ebisawa, T. Toyama, Y. Nagai, M. Fukuda, T. Miyazawa, T. Tanaka, S. Nogami, Effect of neutron irradiation on rhenium cluster formation in tungsten and tungsten-rhenium alloys, J. Nucl. Mater. 507 (2018) 78–86, https://doi.org/10.1016/J.JNUCMAT.2018.04.031.

[15] X. Hu, C.M. Parish, K. Wang, T. Koyanagi, B.P. Eftink, Y. Katoh, Transmutation-induced precipitation in tungsten irradiated with a mixed energy neutron spectrum, Acta Mater. 165 (2019) 51–61, https://doi.org/10.1016/j.actamat.2018.11.032.

[16] L.M. Garrison, Y. Katoh, N.A.P.K. Kumar, Mechanical properties of single-crystal tungsten irradiated in a mixed spectrum fission reactor, J. Nucl. Mater. 518 (2019) 208–225, https://doi.org/10.1016/J.JNUCMAT.2019.02.050.

[17] Y. Katoh, L.L. Snead, L.M. Garrison, X. Hu, T. Koyanagi, C.M. Parish, P. D. Edmondson, M. Fukuda, T. Hwang, T. Tanaka, A. Hasegawa, Response of unalloyed tungsten to mixed spectrum neutrons, J. Nucl. Mater. 520 (2019) 193–207, https://doi.org/10.1016/j.jnucmat.2019.03.045.

[18] M. Dürrschnabel, M. Klimenkov, U. Jäntsch, M. Rieth, H.C. Schneider, D. Terentyev, New insights into microstructure of neutron-irradiated tungsten, Sci. Rep. 11 (2021) 1–17, https://doi.org/10.1038/s41598-021-86746-6, 2021 11:1.

[19] A. Chauhan, Q. Yuan, D. Litvinov, E. Gaganidze, H.C. Schneider, D. Terentyev, J. Aktaa, Effect of temperature on the neutron irradiation-induced cavities in tungsten, 10.1080/14786435.2022.2079750. 102 (2022) 1665–1683. doi:10.1080/14786435.2022.2079750.

[20] M. Klimenkov, U. Jäntsch, M. Rieth, H.C. Schneider, D.E.J. Armstrong, J. Gibson, S. G. Roberts, Effect of neutron irradiation on the microstructure of tungsten, Nucl. Mater. Energy 9 (2016) 480–483, https://doi.org/10.1016/j.nme.2016.09.010.

[21] M. Klimenkov, M. Dürrschnabel, U. Jäntsch, P. Lied, M. Rieth, H.C. Schneider, D. Terentyev, W. Van Renterghem, Microstructural analysis of W irradiated at different temperatures, J. Nucl. Mater. 572 (2022) 154018, https://doi.org/10.1016/J.JNUCMAT.2022.154018.

[22] D. Papadakis, K. Mergia, E. Manios, V. Chatzikos, S. Dellis, D. Terentyev, G. Bonny, W. van Renterghem, C.C. Chang, S. Messoloras, Defect evolution of neutron irradiated ITER grade tungsten after annealing, Fusion Eng. Des. 189 (2023) 113486, https://doi.org/10.1016/J.FUSENGDES.2023.113486.

[23] S. Dellis, X. Xiao, D. Terentyev, E. Manios, K. Mergia, Hardening mechanisms of "cold" rolled tungsten after neutron irradiation: indentation and finite elements modelling, Int J Refract Metals Hard Mater 111 (2023) 106096, https://doi.org/10.1016/J.IJRMHM.2022.106096.

[24] E. Gaganidze, A. Chauhan, H.C. Schneider, D. Terentyev, G. Borghmans, J. Aktaa, Fracture-mechanical properties of neutron irradiated ITER specification tungsten, J. Nucl. Mater. 547 (2021) 152761, https://doi.org/10.1016/J.JNUCMAT.2020.152761.

[25] L.M. Garrison, Y. Katoh, J.W. Geringer, M. Akiyoshi, X. Chen, M. Fukuda, A. Hasegawa, T. Hinoki, X. Hu, T. Koyanagi, E. Lang, M. McAlister, J. McDuffee, T. Miyazawa, C. Parish, E. Proehl, N. Reid, J. Robertson, H. Wang, PHENIX U.S. Japan collaboration investigation of thermal and mechanical properties of thermal neutron-shielded irradiated tungsten, Fusion Sci. Technol. 75 (2019) 499–509, https://doi.org/10.1080/15361055.2019.1602390.

[26] M. Akiyoshi, L.M. Garrison, J.W. Geringer, H. Wang, A. Hasegawa, S. Nogami, Y. Katoh, Thermal diffusivity of irradiated tungsten and tungsten-rhenium alloys, J. Nucl. Mater. 543 (2021) 152594, https://doi.org/10.1016/J.JNUCMAT.2020.152594.

[27] M.J. Lloyd, A.J. London, J. Haley, M.R. Gilbert, C.S. Becquart, C. Domain, E. Martinez, M. Moody, P.A.J. Bagot, D. Nguyen-Manh, D.E.J. Armstrong, Interaction of transmutation products with precipitates, dislocations and grain boundaries in neutron irradiated W, Materialia (Oxf) (2022) 101370, https://doi.org/10.1016/j.mtla.2022.101370.

[28] M.J. Lloyd, R.G. Abernethy, M.R. Gilbert, I. Griffiths, P.A.J. Bagot, D. Nguyen-Manh, M.P. Moody, D.E.J. Armstrong, Decoration of voids with rhenium and osmium transmutation products in neutron irradiated single crystal tungsten, Scr. Mater. 173 (2019), https://doi.org/10.1016/j.scriptamat.2019.07.036.

[29] W.D. Klopp, Review of ductilizing of group VIA elements by rhenium and other solutes, NASA technical note, Nat. Aeronaut. Space Admin. (1968).

[30] W.D. Klopp, A review of chromium, molybdenum, and tungsten alloys, J. Less Common Met. 42 (1975) 261–278, https://doi.org/10.1016/0022-5088(75)90046-6.

[31] P.L. Raffo, Yielding and fracture in tungsten and tungsten-rhenium alloys, J. Less Common Metals 17 (1969) 133–149, https://doi.org/10.1016/0022-5088(69)90047-2.

[32] S. Watanabe, S. Nogami, J. Reiser, M. Rieth, S. Sickinger, S. Baumgärtner, T. Miyazawa, A. Hasegawa, Tensile and impact properties of tungsten-rhenium alloy for plasma-facing components in fusion reactor, Fusion Eng. Des. 148 (2019) 111323, https://doi.org/10.1016/J.FUSENGDES.2019.111323.

[33] R.W. Harrison, On the use of ion beams to emulate the neutron irradiation behaviour of tungsten, Vacuum 160 (2019) 355–370, https://doi.org/10.1016/j.vacuum.2018.11.050.

[34] R.W. Harrison, G. Greaves, J.A. Hinks, S.E. Donnelly, Intermetallic *Re* phases formed in ion irradiated WRe alloy, J. Nucl. Mater. 514 (2019) 123–127, https://doi.org/10.1016/J.JNUCMAT.2018.11.021.

[35] T. Hwang, M. Fukuda, S. Nogami, A. Hasegawa, H. Usami, K. Yabuuchi, K. Ozawa, H. Tanigawa, Effect of self-ion irradiation on hardening and microstructure of tungsten, Nucl. Mater. Energy 9 (2016) 430–435, https://doi.org/10.1016/j.nme.2016.06.005.

[36] F. Ferroni, X. Yi, K. Arakawa, S.P. Fitzgerald, P.D. Edmondson, S.G. Roberts, High temperature annealing of ion irradiated tungsten, Acta Mater. 90 (2015) 380–393, https://doi.org/10.1016/j.actamat.2015.01.067.

[37] F. Luo, H. Luo, Q. Liu, L. Zhou, W. Lin, Z. Xie, L. Guo, The effect of rhenium content on microstructural changes and irradiated hardening in W-*Re* alloy under high-dose ion irradiation, Nanomaterials 13 (2023) 497, https://doi.org/10.3390/NANO13030497. Page13 (2023) 497.

[38] F. Luo, L. Guo, D. Lu, J. Wang, Z. Zheng, W. Zhang, Z. Shen, TEM observation of bubbles induced by single and sequential He/H irradiation in tungsten, Fusion Eng. Des. 125 (2017) 463–467, https://doi.org/10.1016/J.FUSENGDES.2017.04.014.

[39] J. Matolich, H. Nahm, J. Moteff, Swelling in neutron irradiated tungsten and tungsten-25 percent rhenium, Scr. Metall. 8 (1974) 837–841.

[40] D. Nguyen-Manh, M. Klimenkov, M.J. Lloyd, J.S. Wr, Transmutation effects on microstructure of radiation damage in tungsten under neutron irradiation, In Preparation. (n.d.).

[41] A. Xu, D.E.J. Armstrong, C. Beck, M.P. Moody, G.D.W. Smith, P.A.J. Bagot, S. G. Roberts, Ion-irradiation induced clustering in W-*Re*-Ta, W-*Re* and W-Ta alloys: an atom probe tomography and nanoindentation study, Acta Mater. 124 (2017) 71–78, https://doi.org/10.1016/J.ACTAMAT.2016.10.050.

[42] A. Xu, C. Beck, D.E.J. Armstrong, K. Rajan, G.D.W. Smith, P.A.J. Bagot, S. G. Roberts, Ion-irradiation-induced clustering in W-*Re* and W-*Re*-Os alloys: a comparative study using atom probe tomography and nanoindentation measurements, Acta Mater. 87 (2015) 121–127, https://doi.org/10.1016/j.actamat.2014.12.049.

[43] E.R. Reese, N. Almirall, T. Yamamoto, S. Tumey, G.Robert Odette, E.A. Marquis, Dose rate dependence of Cr precipitation in an ion-irradiated Fe[*sbnd*]18Cr alloy, Scr. Mater. 146 (2018) 213–217, https://doi.org/10.1016/j.scriptamat.2017.11.040.

[44] S.J. Zinkle, L.L. Snead, Opportunities and limitations for ion beams in radiation effects studies: bridging critical gaps between charged particle and neutron irradiations, Scr. Mater. 143 (2018) 154–160, https://doi.org/10.1016/J.SCRIPTAMAT.2017.06.041.

[45] D. Nguyen-Manh, A.P. Horsfield, S.L. Dudarev, Self-interstitial atom defects in bcc transition metals: group-specific trends, Phys. Rev. B Condens. Matter. Mater. Phys. 73 (2006) 4–7, https://doi.org/10.1103/PhysRevB.73.020101.

[46] T. Suzudo, M. Yamaguchi, A. Hasegawa, Migration of rhenium and osmium interstitials in tungsten, J. Nucl. Mater. 467 (2015) 418–423, https://doi.org/10.1016/j.jnucmat.2015.05.051.

[47] T. Suzudo, M. Yamaguchi, A. Hasegawa, Stability and mobility of rhenium and osmium in tungsten: first principles study, Model. Simul. Mat. Sci. Eng. 22 (2014), https://doi.org/10.1088/0965-0393/22/7/075006.

[48] T. Suzudo, A. Hasegawa, Suppression of radiation-induced point defects by rhenium and osmium interstitials in tungsten, Sci. Rep. 6 (2016) 1–6, https://doi.org/10.1038/srep36738.

[49] N. Castin, P. Dwivedi, L. Messina, A. Bakaev, D. Terentyev, G. Bonny, The effect of rhenium on the diffusion of small interstitial clusters in tungsten, Comput. Mater. Sci. 177 (2020) 109580, https://doi.org/10.1016/j.commatsci.2020.109580.

[50] M.J. Lloyd, R.G. Abernethy, D.E.J. Armstrong, P.A.J. Bagot, M.P. Moody, E. Martinez, D. Nguyen-Manh, Radiation-induced segregation in W-*Re*: from kinetic Monte Carlo simulations to atom probe tomography experiments, Eur. Phys. J. B 92 (2019), https://doi.org/10.1140/epjb/e2019-100244-y.

[51] C.H. Huang, L. Gharaee, Y. Zhao, P. Erhart, J. Marian, Mechanism of nucleation and incipient growth of *Re* clusters in irradiated W-*Re* alloys from kinetic Monte Carlo simulations, Phys. Rev. B 96 (2017) 1–18, https://doi.org/10.1103/PhysRevB.96.094108.

[52] C.H. Huang, J. Marian, A generalized Ising model for studying alloy evolution under irradiation and its use in kinetic Monte Carlo simulations, J. Phys. Condens. Matter 28 (2016), https://doi.org/10.1088/0953-8984/28/42/425201.

[53] J.S. Wróbel, D. Nguyen-Manh, K.J. Kurzydłowski, S.L. Dudarev, A first-principles model for anomalous segregation in dilute ternary tungsten-rhenium-vacancy alloys, J. Phys. Condens. Matter 29 (2017), https://doi.org/10.1088/1361-648X/aa5f37.

[54] M.J. Lloyd, E. Martinez, L. Messina, D. Nguyen-Manh, Development of a solute and defect concentration dependant Ising model for the study of transmutation induced segregation in neutron irradiated W-(*Re*, Os) systems, J. Phys. Condens. Matter 33 (2021), https://doi.org/10.1088/1361-648X/ac1ec4.

[55] A. Giannattasio, S.G. Roberts, Strain-rate dependence of the brittle-to-ductile transition temperature in tungsten, Philos. Mag. 87 (2007) 2589–2598, https://doi.org/10.1080/14786430701253197.

[56] M. Fleming, T. Stainer, M. Gilbert, The FISPACT-II User Manual UKAEA-R(18)001, UK Atomic Energy Authority, 2018.

[57] A. E521, Standard practice for neutron radiation damage simulation by charged-particle, in: Annual Book of ASTM Standards, 12.02, 2009, pp. 1–21, https://doi.org/10.1520/E0521-96R09E02.Copyright.

[58] S. Agarwal, Y. Lin, C. Li, R.E. Stoller, S.J. Zinkle, On the use of SRIM for calculating vacancy production: quick calculation and full-cascade options, Nucl. Instrum. Methods Phys. Res. B 503 (2021) 11–29, https://doi.org/10.1016/j.nimb.2021.06.018.

[59] W.C. Oliver, G.M. Pharr, An improved technique for determining hardness and elastic modulus using load and displacement sensing indentation experiments, J. Mater. Res. 7 (1992) 1564–1583, https://doi.org/10.1557/JMR.1992.1564.

[60] J.S. Weaver, C. Sun, Y. Wang, S.R. Kalidindi, R.P. Doerner, N.A. Mara, S. Pathak, Quantifying the mechanical effects of He, W and He + W ion irradiation on tungsten with spherical nanoindentation, J. Mater. Sci. 53 (2018) 5296–5316, https://doi.org/10.1007/s10853-017-1833-8.

[61] L.A. Giannuzzit, J.L. Drownt, S.R. Brown, R.B. Irwin, F.A. Stevie, FOCUSED ion beam milling for site specific scanning and transmission electron microscopy specimen preparation, (1927). doi:10.1017/S143192760000862X.

[62] M.L. Jenkins, M.A. Kirk, Characterisation of radiation damage by transmission electron microscopy, (2000). doi:10.1201/9781420034646.

[63] P. Thévenaz, U.E. Ruttimann, M. Unser, A pyramid approach to subpixel registration based on intensity, IEEE Trans. Image Process. 7 (1998) 27–41, https://doi.org/10.1109/83.650848.

[64] D.R.G. Mitchell, Dave Mitchell's DigitalMicrograph™ Scripting Website, (n.d.). http://www.dmscripting.com/meanfreepathestimator.html.

[65] T. Malis, S.C. Cheng, R.F. Egerton, EELS log-ratio technique for specimen-thickness measurement in the TEM, J. Electron Microsc. Tech. 8 (1988) 193–200, https://doi.org/10.1002/JEMT.1060080206.

[66] B, M.M. P, C.J. M, R.S.P. Gault, Atom Probe Tomography, Springer Science & Business Media, 2012.

[67] A. Leach, D.J. Jones, The preparation and some properties of tungsten-rhenium-osmium alloys, Powder Metall. 10 (1967) 174–191, https://doi.org/10.1179/pom.1967.10.20.007.

[68] C. Fletcher, M.P. Moody, C. Fleischmann, M. Dialameh, C. Porret, B. Geiser, D. Haley, Automated calibration of model-driven reconstructions in atom probe tomography, J. Phys. D Appl. Phys. 55 (2022) 375301, https://doi.org/10.1088/1361-6463/AC7986.

[69] C. Fletcher, M.P. Moody, D. Haley, Towards model-driven reconstruction in atom probe tomography, J. Phys. D Appl. Phys. 53 (2020), https://doi.org/10.1088/1361-6463/abaaa6.

[70] K. Lindgren, P. Dömstedt, P. Szakalos, M. Thuvander, The nanostructure of the oxide formed on Fe-10Cr-4Al exposed in liquid Pb, Microsc. Microanal. 28 (2022) 1321–1334, https://doi.org/10.1017/S1431927621000337.

[71] P.D. Edmondson, C.M. Parish, Y. Zhang, A. Hallén, M.K. Miller, Helium bubble distributions in a nanostructured ferritic alloy, J. Nucl. Mater. 434 (2013) 210–216, https://doi.org/10.1016/J.JNUCMAT.2012.11.004.

[72] X. Wang, C. Hatzoglou, B. Sneed, Z. Fan, W. Guo, K. Jin, D. Chen, H. Bei, Y. Wang, W.J. Weber, Y. Zhang, B. Gault, K.L. More, F. Vurpillot, J.D. Poplawsky, Interpreting nanovoids in atom probe tomography data for accurate local compositional measurements, Nat. Commun. 11 (2020) 1–11, https://doi.org/10.1038/s41467-020-14832-w.

[73] X. Wang, K. Jin, D. Chen, H. Bei, Y. Wang, W.J. Weber, Y. Zhang, J. Poplawsky, K. L. More, Investigating effects of alloy chemical complexity on helium bubble formation by accurate segregation measurements using atom probe tomography, Microsc. Microanal. 25 (2019) 1558–1559, https://doi.org/10.1017/S1431927619008523.

[74] W.T. Lin, G.M. Yeli, G. Wang, J.H. Lin, S.J. Zhao, D. Chen, S.F. Liu, F.L. Meng, Y. R. Li, F. He, Y. Lu, J.J. Kai, He-enhanced heterogeneity of radiation-induced segregation in FeNiCoCr high-entropy alloy, J. Mater. Sci. Technol. 101 (2022) 226–233, https://doi.org/10.1016/J.JMST.2021.05.053.

[75] D. Papadakis, S. Dellis, V. Chatzikos, E. Manios, I.E. Stamatelatos, S. Messoloras, K. Mergia, Neutron irradiation effects in different tungsten microstructures, Phys. Scr. 96 (2021) 124041, https://doi.org/10.1088/1402-4896/ac1eb2.

[76] J. Marian, C.S. Becquart, C. Domain, S.L. Dudarev, M.R. Gilbert, R.J. Kurtz, D. R. Mason, K. Nordlund, A.E. Sand, L.L. Snead, T. Suzudo, B.D. Wirth, Recent advances in modeling and simulation of the exposure and response of tungsten to fusion energy conditions, Nucl. Fusion 57 (2017) 092008, https://doi.org/10.1088/1741-4326/AA5E8D.

[77] A. Chauhan, Q. Yuan, D. Litvinov, E. Gaganidze, H.C. Schneider, D. Terentyev, J. Aktaa, Effect of temperature on the neutron irradiation-induced cavities in tungsten, Philos. Mag. 102 (2022) 1665–1683, https://doi.org/10.1080/14786435.2022.2079750.

[78] G.S. WAS, Fundamentals of Radiation Materials Science, Springer, New York, New York, NY, 2017, https://doi.org/10.1007/978-1-4939-3438-6.

[79] T. Suzudo, A. Hasegawa, Suppression of radiation-induced point defects by rhenium and osmium interstitials in tungsten, Sci. Rep. 6 (2016) 1–6, https://doi.org/10.1038/srep36738, 2016 6:1.

[80] Y.H. Li, F.Y. Yue, Z.Z. Li, P.W. Hou, Y.Z. Niu, H.Z. Ma, Y. Zhang, X.X. Hu, H. Q. Deng, H.B. Zhou, F. Gao, G.H. Lu, Temperature-dependent synergistic evolution mechanism of rhenium and irradiation defects in tungsten-rhenium alloys, J. Mater. Sci. Technol. 145 (2023) 221–234, https://doi.org/10.1016/J.JMST.2022.10.056.

[81] Y. Liu, Y. Song, P. Zhang, S. Wang, T. Zhu, S. Jin, E. Lu, X. Cao, B. Wang, The influence of rhenium addition on the distribution of vacancy-type defects in tungsten, J. Nucl. Mater. 553 (2021), https://doi.org/10.1016/j.jnucmat.2021.153045.